Available online at www.sciencedirect.com

jmr&t Journal of Materials Research and Technology

journal homepage: www.elsevier.com/locate/jmrt

Original Article

Study on location-related thermal cycles and microstructure variation of additively manufactured inconel 718

Tao Zhang [a,b], Huigui Li [a,b], Hai Gong [a,b,*], Yunxin Wu [a,b], Xin Chen [c], Xiaoyong Zhang [d]

[a] Light Alloy Research Institute, Central South University, Changsha 410083, China
[b] State Key Laboratory of High Performance Complex Manufacturing, Central South University, Changsha 410083, China
[c] Welding Engineering and Laser Processing Centre, Cranfield University, Bedford, MK43 0AL, UK
[d] School of Materials Science and Engineering, Nanjing University of Science and Technology, Nanjing, 210094, China

ARTICLE INFO

Article history:
Received 8 January 2022
Accepted 28 March 2022
Available online 4 April 2022

Keywords:
Wire + arc additive manufacture
Cold rolling
Thermal cycles
Microstructure
Grain transformation mechanism

ABSTRACT

The complicated thermal history of wire + arc additive manufacturing (WAAM) will affect the microstructure variation and mechanical properties of the as-deposited material. Numerial models of Inconel 718 in WAAM deposition were established and the location-related thermal history and temperature distribution were analyzed. A hybrid method of WAAM and cold rolling was investigated and its effect on the microstructure distribution and texture was investigated compared to that in as-deposited condition. The results show that WAAM deposition features repeated thermal cycles, high heating rate and low cooling rate. The trough values of the thermal cycles first increases and then decreases, while the peak temperature always decreases with the proceeding of the deposition process. The as-deposited samples show columnar dendrites and its average dendrite arm spacing increases with the increased build height due to the location-related heat accumulation. The strongly textured columnar dendrites with preferred <001> orientation transform to equiaxed grains with random orientation in heat-affected zone after cold rolling process, and its average size decreases with the increased rolling force. The as-deposited samples show the strongest intensity of 7.609 for the {100} family of grains oriented along the transverse direction; while it decreases to 3.629 and 2.057 for the cold rolled conditions with the force of 50 kN and 75 kN, respectively. The relationship between thermal history and the microstructure distribution was discussed. The mechanism of hybrid WAAM and cold rolling method consisted of spatially and temporally heterogeneous work hardening and recrystallization.

© 2022 The Author(s). Published by Elsevier B.V. This is an open access article under the CC BY-NC-ND license (http://creativecommons.org/licenses/by-nc-nd/4.0/).

* Corresponding author.
E-mail address: gonghai@csu.edu.cn (H. Gong).

https://doi.org/10.1016/j.jmrt.2022.03.178

2238-7854/© 2022 The Author(s). Published by Elsevier B.V. This is an open access article under the CC BY-NC-ND license (http://creativecommons.org/licenses/by-nc-nd/4.0/).

1. Introduction

Inconel 718 (IN-718) is the key material for the manufacture of aerospace components due to its high strength and thermal ability at high temperature [1–3]. IN-718 is a precipitation hardening Ni–based superalloy and it is strengthened by relying on γ" [Ni_3Nb] phase as the primary strengthener phase and γ' [$Ni_3(Al, Ti)$] as the secondary one [4–7]. Wire and Arc Additive Manufacturing (WAAM) is a popular AM technique that allows for the rapid manufacturing of large metallic parts with a high deposition rate and low equipment cost [8,9]. The ability to use wire as the feedstock material increases the efficiency of the process when compared to powder-based techniques by avoiding the necessity for constrained build volumes and powder recycling [10]. WAAM enables over 10-times the volumetric deposition rates of powder-based AM processes. However, the high depositions rates of WAAM require high heat input to melt the large volume of material, which in turn results in potential flaws such as pores, cracks, distortion, loss of mechanical properties and low dimensional accuracy [11]. The metal wire is melted layer-by-layer using an electric arc, and near-net shape parts of meter-scale structural components can be manufactured in WAAM without the limitation of the vacuum chamber of the powder bed fusion [12,13].

Studies on the thermal cycles and microstructure of the WAAM deposited material have been reported [14,15]. Due to the complicated thermal history of the material in the layer-by-layer WAAM deposition, numerical simulation was widely adopted to study the temperature variation. The transient heat and fluid flow were critical during fusion-based additive manufacturing, since they impacted the as-built microstructure. Ke [16] studied the temperature and velocity fields of the molten pool in WAAM deposition with the development of the force, surface Gauss heat source and periodic droplet transfer models, which considered the gravity, buoyancy, electromagnetic, surface tension, arc pressure and arc shear stress. Graf et al. [17] investigated the influence of the wire feed and the weld path orientation (unidirectional or continuous) on the temperature evolution and distortions for multi-layered walls. Singh et al. [18] developed a transient 3D finite-element model to study the temperature distribution and disparities in melt-pool behaviours under similar processing conditions in laser additive manufacturing. The temperature and melt-pool increased as laser power moved in the same layer and when new layers were added. There may be phase transformation during the WAAM deposition process, which affected the temperature distribution of the as-deposited materials. Manurung et al. [19] studied the influence of material property model on the distortion of the deposited components. The new property models were generated with advanced material modelling software JMATPRO based on chemical compositions, and the phase-change phenomena was defined in latent heat. Ding et al. [20] proposed a well-distributed heat source model, the computational efficiency was significantly improved by the proposed new method. The residual stress of WAAM deposited wall varied under clamp state and the unclamp conditions. The longitudinal residual stress was tensile along with the wall height and it was compressive at the substrate under the clamping state, while it was redistributed after unclamping and the maximum longitudinal tensile residual stress was generated on the contact area between the deposited wall and the substrate. In the clamped condition, longitudinal residual stresses was near the as-deposited yield strength and virtually constant along the wall height, which allowed the sample to distort after unclamping. Large residual stress was the main factor for the distortion of the additively manufactured components. Sun et al. [21] performed a number of numerical simulations to analyze the distribution characteristics of residual stress in the WAAM components made of aluminum alloy. The results showed that the variation in the height of beam can affect the magnitude and distribution of longitudinal residual stress in both the substrate and the beam. The interlayer dwell time was believed to have an effect on residual stress distributions due to variance in heat dissipation condition [22]. Fang et al. [23] investigated the effect of characteristic substrate parameters, including the length, width, thickness and initial temperature, on the minimum temperature during the first pass deposition, which was essential to find out when and how to adjust the processing parameters according to the characteristic parameters of the deposited part. Li et al. [24] studied the role of dwell time between layers on the thermal stress evolutions and residual stress distributions of the thin-walled component and substrate in WAAM. The results showed that with the interlayer dwell time, the stress cycling curves became more uniform and the interlayer stress-releasing effect was weakened. The residual stress levels on the substrate also decreased with the increased interlayer dwell time. Substrate preheating was an efficient approach to decrease the thermal stress and cracking of components. Knezovi et al. [25] studied the relationship between interlayer temperature and process duration and to determine the influence of the interlayer temperature on product structure and other properties. Xiong et al. [26] established a 3D transient heat transfer model of a circular ten-layer single-pass part, and found that substrate preheating could make the thermal cycles much smoother and decrease the cooling rate of the molten pool. The maximum temperature gradient in the molten pool also decreased with increased substrate preheating temperature. Benakis [27] explored the effects of the frequency of pulsed current on the weld-bead geometry and heat affected zone in gas tungsten arc welding (GTAW). The results demonstrated the ability to control both the weld-bead dimensions and penetration depth, as well as the heat affected regions by utilizing the dual pulsing combination of both high and low frequency pulsing.

Apart from the residual stress and distortion, the location-related thermal history in WAAM will also affect the microstructure, the quality of deposition and mechanical properties of the components [28]. Wu et al. [29] investigated the influence of heat accumulation on bead formation, arc stability, and metal transfer behaviour during the WAAM deposition of Ti6Al4V using localized gas shielding. The results showed that there existed a significant difference in temperature variation between the substrate and in-situ layer due to the various thermal dissipation paths along the building height. Owing to the influences of heat accumulation, the interlayer surface

oxidation and bead geometries varied along the building direction, especially for the first few layers of the deposited wall. Rodrigues et al. [30] found that the microstructure and mechanical properties of the as-built parts were correlated with the thermal cycles as the heat input affected the cooling rates, interlayer temperatures, and residence times. Kindermann et al. [31] investigated the effects of processing parameters and heat treatments employed on CMT-WAAM of a precipitation hardenable IN-718 and found the localized regions with high microhardness near interlayer regions due to a local dissolution of Nb-rich eutectic phases. Ge et al. [32] adopted the transient thermal transfer model and the thermal elastic–plastic model for the thermal and stress simulation during the additively manufacture of 2Cr13 thin-wall part. The spatially transient thermal distribution during the arc deposition process induced the formation of the corresponding transient stress fields. The position of the maximum transient normalized stress, located near the top layer and both ends of the deposit, evolved regularly with the continuously deposition of new layer on the top surface. This regular alternately-transformed phenomenon was primarily in connection with the constantly reheating and cooling processes while depositing new layer on its top surface. The location-related metal-stable microstructure and nonhomogeneous micro-sized pore distribution was obtained due to the in-situ micro-heating treatment of the new layers deposition. Hejripour et al. [33] revealed the correlation between the calculated cooling rates and the phases formation in the WAAM parts of duplex stainless steel. The results showed that slow cooling rate (below 50 °C/s) of the built layers at elevated temperatures significantly promoted austenite formation in a ferrite matrix. Tanvir et al. [34] studied the phase stability and mechanical properties of as-deposited H13 tool steel at elevated temperatures. The location-dependent phase combinations were observed, which could be explained by nonequilibrium thermal cycles that resulted from the layer-by-layer stacking mechanism used in WAAM. Gao et al. [35] investigated the microstructure and mechanical properties in the different locations of the additively manufactured 9Cr ferritic/martensitic wall. The differences in the mechanical properties were related to the anisotropy in microstructure with the increased height of the wall. Different heat accumulation will change the microstructure along the build direction of the built components. Bai et al. [36] studied the thermal cycles of 2219 aluminum alloy during gas tungsten arc welding based additive manufacturing. The thermal cycles can be classified into three categories: melting heat, partial-melting heat and post-heat based on the consequences and time sequences, thus resulting in the distinct microstructure characteristic at the top and bottom regions of the components. The concentration of the temperature may lead to deteriorating the quality of deposition. The developed model proposed by Gokhale [37] can be used further for the development of the feedback-based temperature management system to provide smooth metal deposition with better quality. Geng et al. [38] constructed a model composed of a macroscopic finite element (FE) model combined with a microscopic phase field model to investigate the Al alloy microstructure evolution during WAAM. The FE model was implemented to calculate the temperature gradient and solidification speed under different processing parameters, and these results were then fed into the phase field (PF) model to simulate the microstructure and concentration field of chemical compositions.

However, the research focusing on the thermal cycles of WAAM deposited IN-718 was rarely published. Additionally, the correlation between the thermal cycles and the microstructure variation (morphology and size of the grains as well as the secondary phases) as well as its distribution of IN-718 had not been extensively investigated. In this study, numerical models of WAAM deposition of IN-718 was established and its location-related thermal cycles and temperature distribution were investigated. Thermocouples and infrared camera were adopted to monitor and validate the temperature variation. The effect of thermal history on the microstructure distribution, including the grains transformation, texture and the precipitates was analyzed. Furthermore, inter-layer cold rolling was integrated into the WAAM deposition and its effect on the microstructure and texture variation was comparatively studied. The relationship between thermal cycles and the microstructure variation, as well as the mechanism of the grains transformation were discussed.

2. Material and methods

Two different methods were comparatively conducted to built the sample in this study: WAAM deposited and inter-layer cold rolled. Fig.1 shows the schematic diagram of hybrid WAAM deposition and cold rolling technology. WAAM deposition was achieved by the layer-by-layer deposition using the welding technology of cold metal transfer (CMT). The WAAM deposition system consists of a CMT welding power source (Fronius, CMT 4000 advanced), a wire feeder (Fronius, VR 7000 CMT) and a CMT torch. The diameter of the IN-718 wire used was 1.2 mm and its compositions (wt.%) are: 53.15 Ni - 19.42 Cr - 5.22 Nb + Ta - 2.95 Mo - 0.96 Ti - 0.47 Al - 0.41 Cu - 0.11 Mn – Bal. Fe.

The parameters of CMT deposition of IN-718 were described as follows: contact tip-to-work distance was 14 mm, the torch travel speed and wire feed speed were 3.6 m/min and 7 m/min, respectively. The inter-layer dwell time was 3 min to cool down the previously deposited material. Pure argon was adopted as the shielding gas for the local protection of the CMT deposition and its flow rate was 15 L/min. The hybrid WAAM deposition and cold rolling was composed of alternative one-layer deposition and one-layer cold rolling process. The roller was applied on the top surface of the deposited material with different rolling forces (0, 50, 75 kN) when the temperature on the top surface cooled down with 3 min. The diameter and width of the roller were 100 mm and 20 mm, respectively.

Three comparative walls with 20 layers were built: as-deposited (AD), cold-rolled (CR) with the rolling force of 50 kN and 75 kN, respectively. Three thermocouples were attached to one side of the walls to record the temperature variation during the WAAM deposition, meanwhile, infrared camera was also adopted to monitor the overall temperature distribution of the wall, as shown in Fig. 2. Zig-zag deposition path was adopted in this study to obtain uniform height at both ends of the wall. After the deposition, the microstructure

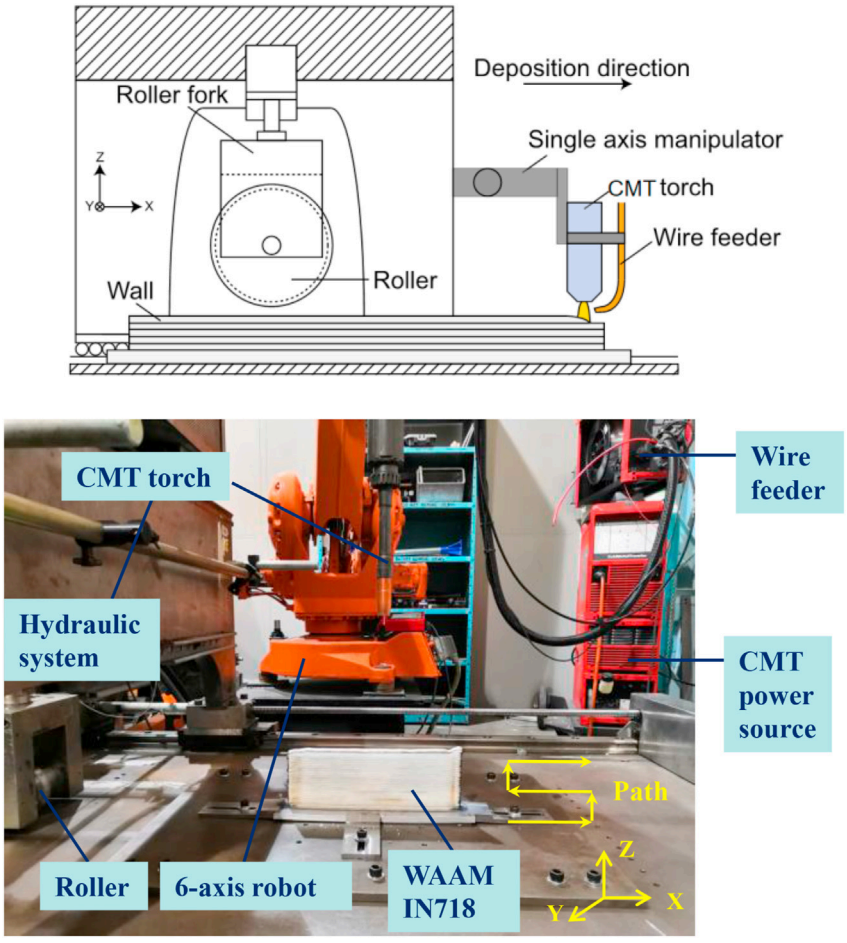

Fig. 1 – Schematic diagram and experimental setup of hybrid WAAM deposition and cold rolling.

of the specimens on the Y-Z plane (perpendicular to the travel direction of the torch) were analyzed. The grain morphology and the distribution of the precipitates were analyzed using optical microscopy (OM) and scanning electron microscopy (SEM) with an energy dispersive spectrometry (EDS). Additionally, the grain orientation and the texture were characterized by electron backscatter diffraction (EBSD) analysis. The HV hardness measurement was conducted through the height direction (Z direction in Fig. 2) of the walls under a load of 1 Kg and a holding time of 15 s. Several tensile coupons were extracted in the horizontal direction (X) of the walls at all conditions. The tensile tests at room temperature with a crosshead speed of 1 mm/min were conducted by electro-mechanical machine (Instron 5500 R). Heat treatment was applied to the specimens for all conditions and its effect on the distribution of the precipitates was investigated. The procedures of the heat treatment were described as follows: solution treated at 970 °C for 1 h followed by water quenching immediately; aging treated at 720 °C for 8 h, and furnace cooled to 620 °C followed by air cooling.

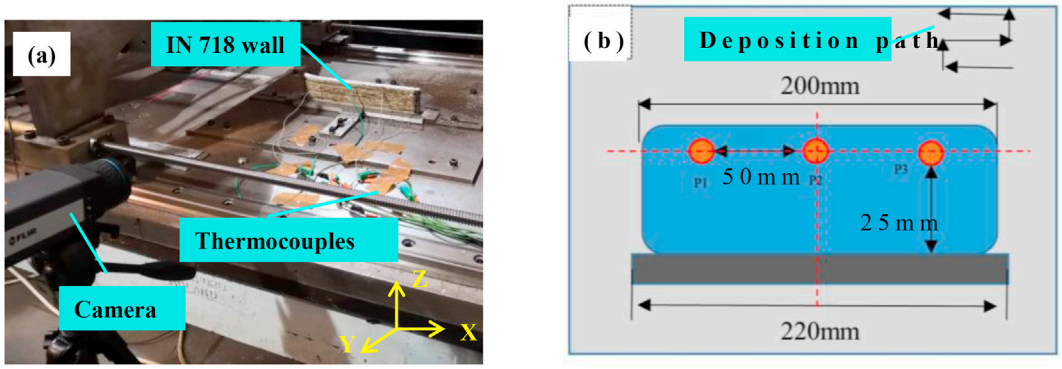

Fig. 2 – Experimental set up flame heating process: (a) thermal couples and infrared camera; (b) location of thermal couples.

3. Numerical simulation analysis

3.1. Geometry determination

The geometry characteristic (including the height and width of each deposited layer) is essential for the accuracy of the numerical simulation. Fig. 3 shows the sectional dimension of the walls under different conditions. It should be noted that the total height of the walls is different and Fig. 3 only shows part of the walls with 20 layers. The width increases from 10.65 mm in the as-deposited condition to 11.05 mm and 11.93 mm in cold rolled samples with the force of 50 kN and 75 kN, respectively. Meanwhile, the cold rolling decreases the average height of each layer, and it decreases with the increased rolling force, as shown in Table 1. Obvious transverse deformation is generated during the rolling process as there is no constraint in the transverse direction of the walls.

3.2. Models description

Based on the characteristics of the WAAM deposition, the first layer shows a smaller layer height compared to that of other deposited layers. The droplet of the first layer is spread out due to its sufficient heat exchange with the cold substrate in all directions; while the subsequent layers show the equal layer height and width due to its directional heat exchange. The geometry of each deposited layer shows an arch shape instead of an rectangle one, as shown in Fig. 3. The geometry of each layer in the numerial model is set based on the experimental values in Section 3.1, which consists of the average height and width as well as the curvature radius, as shown in Fig. 4. The relationship between the height, width and curvature radius of the first layer is shown in Eq. (1).

$$R = \frac{w^2 + 4h_{1st}^2}{8h_{1st}} \tag{1}$$

where R is the curvature radius, w is the width, h_{1st} is the height of the first layer.

Table 1 – Size and strain of walls.

	Average layer height (mm)	Wall width (mm)
AD	2.82	10.65
CR (50 kN)	2.59	11.05
CR (75 kN)	2.31	11.93

AD: as-deposited; CR: cold-rolled

The double ellipsoidal heat source proposed by Goldak [39] was adopted as the heat source model in this study. The volumetric heat density distribution in the front and rear ellipsoid was shown in Fig. 5 and Eqs. (2)–(5). Table 2 shows the shape parameters of the heat source for the CMT deposition of IN-718 in this study.

$$q_f = \frac{6\sqrt{3}Qf_f}{\pi\sqrt{\pi}a_f bc}\exp\left[-3\left(\frac{x^2}{a_f^2}+\frac{y^2}{b^2}+\frac{z^2}{c^2}\right)\right] \tag{2}$$

$$q_r = \frac{6\sqrt{3}Qf_r}{\pi\sqrt{\pi}a_r bc}\exp\left[-3\left(\frac{x^2}{a_r^2}+\frac{y^2}{b^2}+\frac{z^2}{c^2}\right)\right] \tag{3}$$

$$Q = \eta UI \tag{4}$$

$$f_r + f_f = 2 \tag{5}$$

where q_f and q_r are heat flux in the front and rear ellipsoid, respectively. f_f and f_r are front and rear scaling factor, a_f and a_r are the length of front and rear ellipsoid, b and c are the depth and half width of double-ellipsoidal heat source, Q is the effective heat input, η is thermal efficiency and set as 0.8 for CMT deposition, U and I are voltage and current.

The thermophysical properties, such as the specific heat and the heat conductivity, play a vital role in the temperature variation during the CMT deposition. The relationship between these thermophysical properties and the temperature is shown in Table 3. Additionally, CMT deposition features the dynamic cycles of partial melting and solidification. The liquidus temperature and solidus temperature are 1330 °C and 1225 °C for IN-718, indicating a large range of the temperature

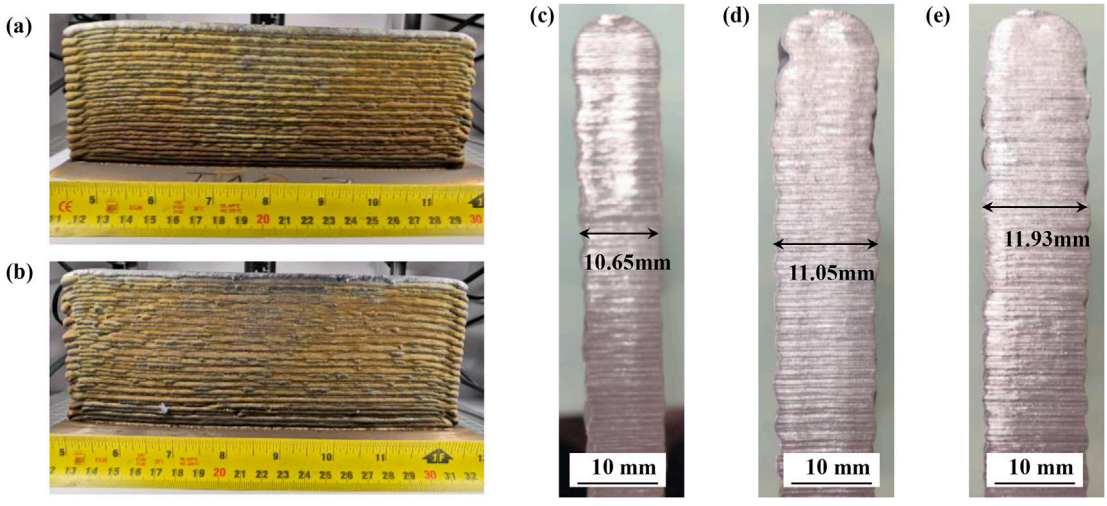

Fig. 3 – Aspects of produced parts: (a) as-deposited wall; (b) Cold rolled wall. Corresponding transverse sections: (c) as-deposited; (d) 50 kN cold-rolled; (e) 75 kN cold-rolled.

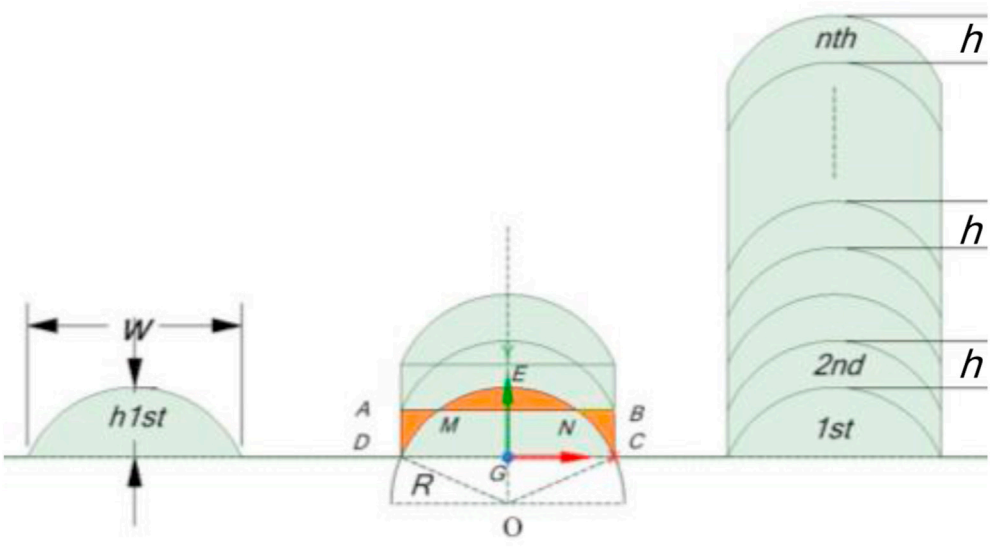

Fig. 4 – Geometry of the numerical models; W is width of the bead, h_{1st} is the height of the 1st layer, h is the average height.

during the deposition of IN-718. The latent heat due to the solidification is considered in this study, and it is set as 250 J/g for IN-718. There is heat exchange between the deposited surface and the environment due to the significant temperature difference. The heat convection (q_c) and radiation (q_r) are defined in Eqs. (6) and (7).

$$q_c = h(T_s - T_e) \tag{6}$$

$$q_r = \varepsilon\beta\left(T_s^4 - T_e^4\right) \tag{7}$$

where h is heat convection coefficient and is set as 20 W/$m^2 \cdot °C$, ε is radiation coefficient and is set as 0.737, which will be discussed in Section 3.4, β is Stefan-Boltzman constant and set as 5.76×10^{-8} W/(m^2 K^4), T_s and T_e are temperatures on the deposited surface and the environment, respectively.

3.3. *Thermal cycles analysis*

Fig.6 shows the temperature distribution during the 1st layer deposition. The size of the molten pool is quite small at the start position, meanwhile, the heat exchange between the deposited material and the substrate is weak. The height at the start position is large due to the heat sink effect at the beginning of the deposition, thus decreasing the welding penetration and leading to the increase of the layer height. The area with high temperature (marked with red color) increases significantly when the torch moves to the middle position, and the molten pool shows double-ellipsoidal shape. The temperature of the substrate increases obviously when the torch moves on. The end position shows the highest temperature due to the short delay of the torch and the

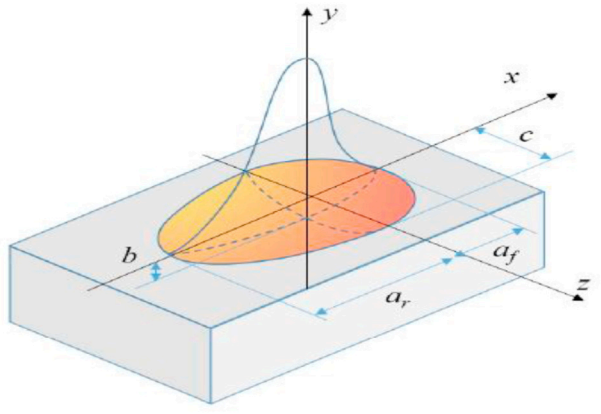

Fig. 5 – Schematic diagram of Goldak's double-ellipsoidal volumetric heat source (the explanation of the parameters is shown in Table 2).

Table 2 – Parameters of the double-ellipsoidal volumetric heat source.

Parameters	Symbol	Values
Voltage	U/V	13.3
Current	I/A	183
Thermal efficiency	H	0.8
Front length [40,41]	a_f/mm	4
Rear length [40,41]	a_r/mm	6
Width	c/mm	5.32
Depth	b/mm	3
Front scaling factor [42]	f_f	0.6
Rear scaling factor [42]	f_r	1.4

Table 3 – Thermophysical properties of IN-718.

Temperature T/°C	Specific heat C_p/(J/kg·°C)	Heat conductivity λ/(W/m·°C)
20	426	11.5
25	429	11.6
100	441	12.8
300	481	14.0
500	520	15.7
700	560	21.6
900	601	24.9
1350	691	31.4
1355	692	31.6

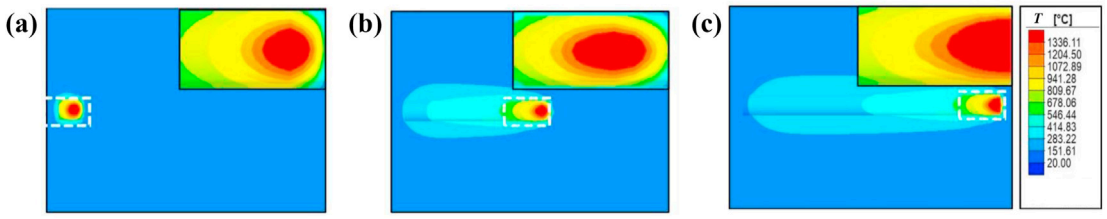

Fig. 6 – Temperature distribution during the 1st layer deposition when the heat source moves on the (a) start position; (b) middle position; (c) end position.

accumulated heat of the previously deposited material. The difficulty of heat dissipation leads to a height decrease at the end position. Zig-zag deposition path was adopted in this study to compensate the height difference between the start and end positions of the deposited layer.

Fig.7 shows the thermal cycles at the center point of different deposited layers. Due to the inherent characteristic of the WAAM deposition, different regions of the deposited layers features a different thermal history. The material is rapidly heated above the melting temperature when the heat source moves in, that is the melting process; then the material is cool down to the room temperature and solidification occurs subsequently; particial melting will take place during the subsequent depositing process. Therefore, the WAAM deposition features high temperature gradient and repeated thermal cycles, resulting in a complicated thermal history. There are 20 peak temperatures of the center point on the 1st layer, corresponding to the 20 layers deposition. The value of the temperature on the first peak is 1550 °C and it exceeds the liquidus temperature, indicating the complete fusion of the material. The temperature of the second peak locates between the solidus and the liquidus temperature, illustrating the partial fusion of the previous deposited material during the subsequent layer deposition. The peak temperature decreases with the proceeding of the deposition process due to the heat exchange and heat conduction. The heat from the top layer is

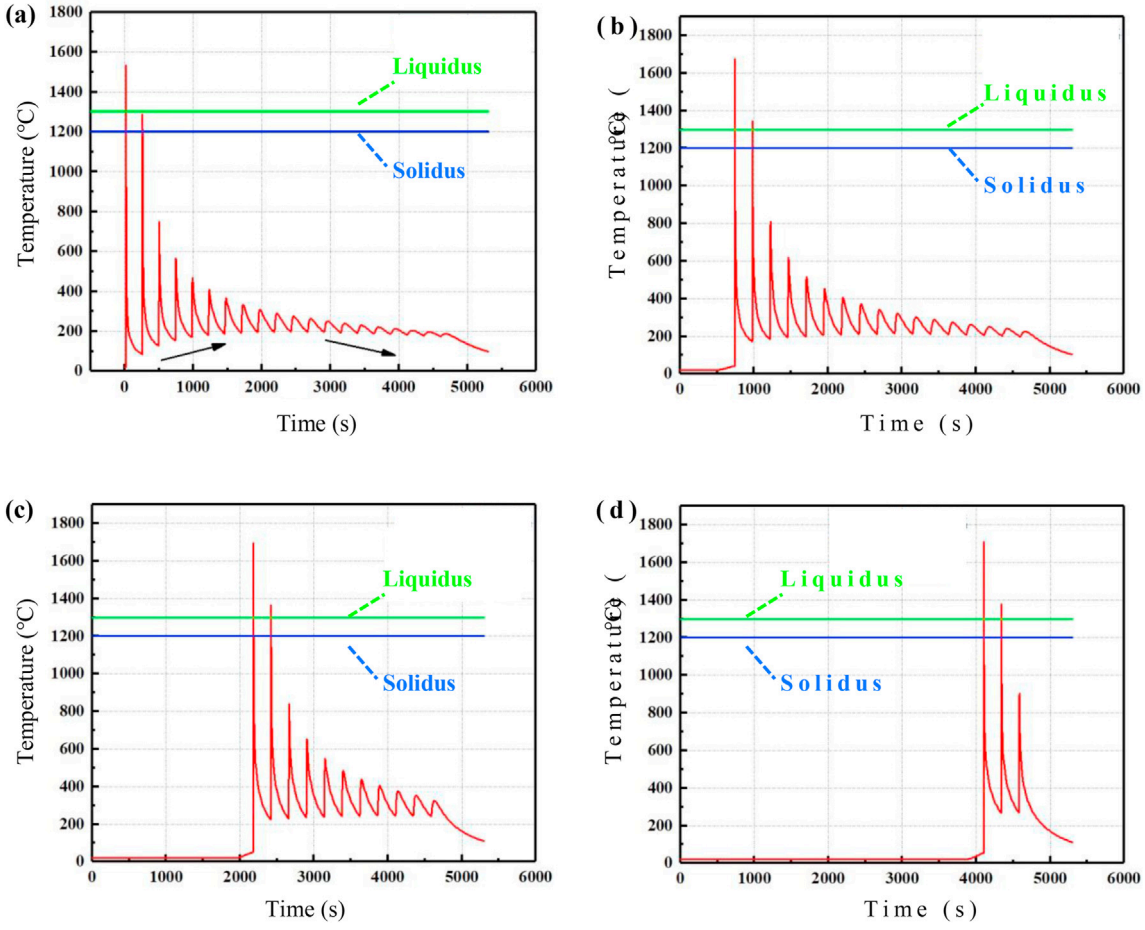

Fig. 7 – Thermal cycles at center point of different deposited layers: (a) 1st layer; (b) 4th layer; (c) 10th layer; (d) 18th layer (The solidus and liquidus of IN718 were also marked).

hardly transferred to the bottom material in a very short time during the subsequent layer deposition, thus significantly decreasing the value of the peak temperature. It is interesting that the trough values of the temperature first increases in the previous ten layers deposition and then decreases with proceeding of the latter ten layers deposition. The trough temperature is quite small during the previous layers due to the sufficient exchange between the deposited material and the cold substrate. The heat input from the subsequent layers will significantly increase the trough temperature as there will be sufficient heat conduction due to the small deposited height. The temperature decrease due to the interpass dwell time can not compensate for the high heat input from the new layers deposition, thus resulting in a temperature increase. Similar to the variation of the peak values, the heat from the top layers can be hardly transmitted to the first layer immediately, thus decreasing the trough values in the deposition of the latter ten layers.

Different additive manufacturing methods show different heating and cooling rate, which results in various microstructure and mechanical properties of the deposited samples. The cooling rates on the order of 10^5–10^6 K s^{-1} can be reached in the powder based additive manufacturing [43], while it is only 10^2–10^4 K s^{-1} for the WAAM deposition [28]. The heating and cooling rates play a vital role in the temperature distribution and the microstructure variation during WAAM deposition. Fig.8 shows the heating and cooling rate at center point of different deposited layers. There are several peaks and troughs for the first layer, however, the heating and cooling rate of the 1st layer both decrease to zero after depositing ten layers. The maximum values of the heating and cooling rate locate at the first peak and trough. The maximum heating rate is 730.8 °C/s for the 1st layer due to the rapid heating from the torch, and it decreases and then changes to negative value gradually when the torch moves away from this position. The maximum cooling rate is 515 °C/s for the 1st layer due to the sufficient heat exchange between the deposited material and the cold substrate as well as the environment. It can be seen that the heating rate is much larger than that of the cooling rate, which is the intrinstic feature of the arc-based additive manufacturing. The heating rate at the center point of the first layer decreases from 730.8 °C/s to 420 °C/s, 208 °C/s, 90 °C/s and 48 °C/s for the subsequent 2nd to 5th layer deposition. It indicates that only the 1st and the 2nd deposition will significantly increase the temperature, while the 3rd to 20th layer deposition mainly provides the transient aging effect to the deposited material in the first layer. The transient aging is quite different from the standard aging treatment for IN-718 due to the limited aging time and the lack of constant temperature. This transient aging may significantly affect the microstructure distribution of the deposited material, which will be discussed in Section 4. Similarly, the cooling rate of the first layer decreases from 515 °C/s to 100 °C/s, 25 °C/s, 10 °C/s and 5 °C/s for the subsequent 2nd to 5th layer

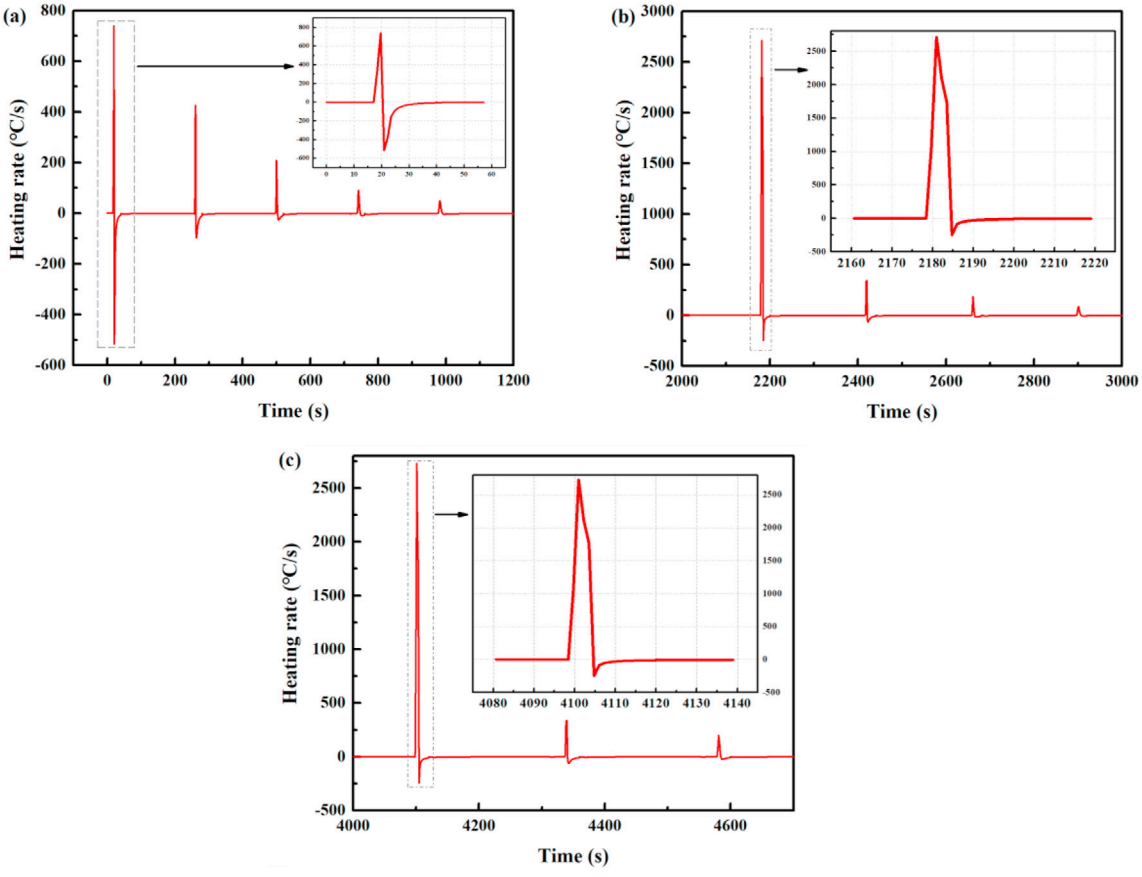

Fig. 8 – Heating and cooling rate at center point of different deposited layers: (a) 1st layer; (b) 10th layer; (c) 18th layer.

deposition. The temperature gradient between the deposited material and the substrate is quite large during the first layer deposition, which leads to sufficient heat exchange and large cooling rate. Nevertheless, the temperature gradient between the previously deposited layer and the new deposited material decreases with the proceeding of the deposition process, thus significantly decreasing the heat exchange and the cooling rate. It can be seen that the cooling rate significantly decreases for the subsequent layer deposition in spite of the interlayer dwell time. As shown in Fig. 8 (b) and (c), the heating rate of the 10th and the 18th layer exceeds 2600 °C/s, which is over three times as that of the first layer; while the cooling rate is less than 250 °C/s and it is only half of that in the first layer. With the proceeding of the deposited layer, the heat accumulation significantly increases and the previous deposited material provides the preheating effect to the subsequent deposited layers, thus increasing the heating rate. The heat accumulation deteriorates the heat exchange conditions, meanwhile, the directional heat conduction due to the increased deposited height will also decrease the cooling rate. Additionally, the preheating effect from the previous deposited material is beneficial to decrease the residual stress by lowering the thermal gradients.

3.4. *Temperature validation*

As presented in Fig. 2, three thermocouples are attached on one side of the walls for the validation of the temperature distribution using the infrared camera. The distance between the thermocouples and the heat source is set as 3.5 mm to avoid the failure of the thermocouples during the new layer deposition. There is oxidation behavior and its extent varies at different positions on the walls during the WAAM deposition. The oxidation behavior will affect the value of the radiation coefficient in the temperature cloud maps using the infrared camera; therefore, it is essential to obtain the accurate values of the radiation coefficient. The radiancy at a given point with a certain temperature is constant, as shown in Eq. (8). Different values have to be set at different points to match the temperature values between the infrared camera and the thermocouples. The experimental values of radiation coefficient can be calculated by Eq. (9). For all the three measuring positions of the thermocouples, five different values of temperature are selected for each position and the average value of radiation coefficient is obtained. As shown in Table 4, as there is large range of the ε3 value compared to that of ε1 and ε2, the maximum and minimum value of ε3 are both removed, the average value of ε3 is revised as 0.75. Therefore, the average value of the radiation coefficient is 0.742.

$$M = \varepsilon\beta T^4 \tag{8}$$

$$\varepsilon_i = \varepsilon_i' T_i'^4 \Big/ T_i^4 \tag{9}$$

where M is radiancy, ε_i (i = 1,2,3) is experimental values of radiation coefficient, ε_i' is the setting value in the infrared camera, T_i' and T_i are temperature values using the infrared camera and the thermocouples, respectively.

Fig.9 shows the comparisons of the temperature variation between the simulated results and the experiment. The simulated temperatures agree with the experimental values and the maximum error of the peak temperature is less than 10%. The error can be explained as follows: firstly, the measuring accuracy of the K-type thermocouples is less than 1%. Additionally, the peak temperature is quite difficult to be identified accurately using the infrared camera.

Table 4 – Calculation of experimental values of radiation coefficient.

	T_1	T_1'	ε_1	T_2	T_2'	ε_2	T_3	T_3'	ε_3
1	355.5	357.3	0.74	324.1	328.4	0.74	381.8	375.4	0.77
2	318.3	316.6	0.69	314.5	310.8	0.75	362.4	361.1	0.72
3	291.2	288.5	0.74	300.9	294.5	0.80	355.4	350.7	0.76
4	271.7	268.5	0.72	274.6	276.2	0.77	331.2	333.0	0.81
5	111.1	110.3	0.69	105.6	107.5	0.74	118.5	113.5	0.61
Averaged ε	0.716			0.76			0.75		

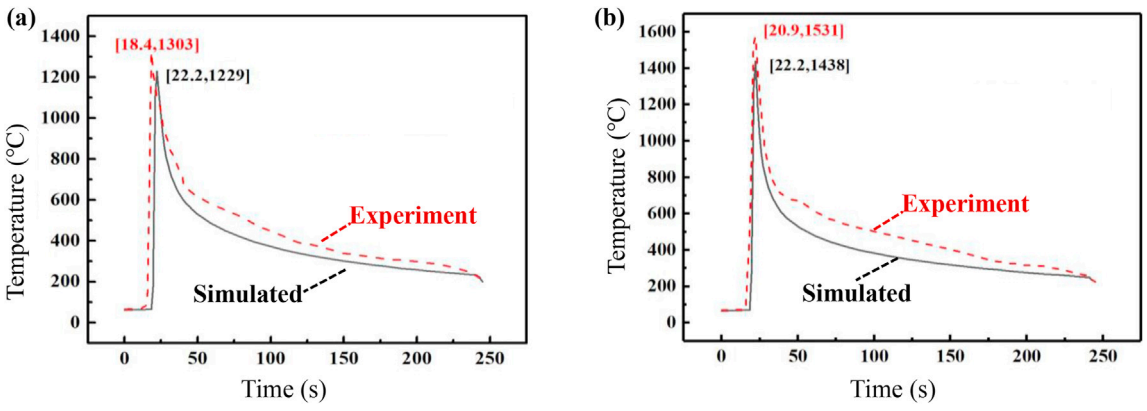

Fig. 9 – Comparisions between experimental and simulated temperature at center points of (a) 10th layer; (b) 20th layer.

4. Microstructure

As shown in Section 3.3, the thermal history in WAAM deposition is quite complex and it is related to the position of the deposited walls. Additionally, the heating and cooling rate are quite different from that in traditional casting or hot forming processes, thus inducing specific and location-related microstructure evolution in WAAM deposition compared to that in cast or wrought materials. Therefore, the microstructure and texture of the as-deposited and cold rolled samples are comparatively investigated and its distribution at different positions of the walls are also analyzed.

4.1. *OM graph*

Fig. 10 shows the microstructure variation in cross section (Y-Z plane) of the as-deposited and cold-rolled samples, which shows fully dense microstructure without defects, such as porosity, cracks or lack of fusion. The coordinate is consistent with that in Fig. 1. Extensively grown columnar dendrites with discrete islands of Laves phase (marked with white arrow)

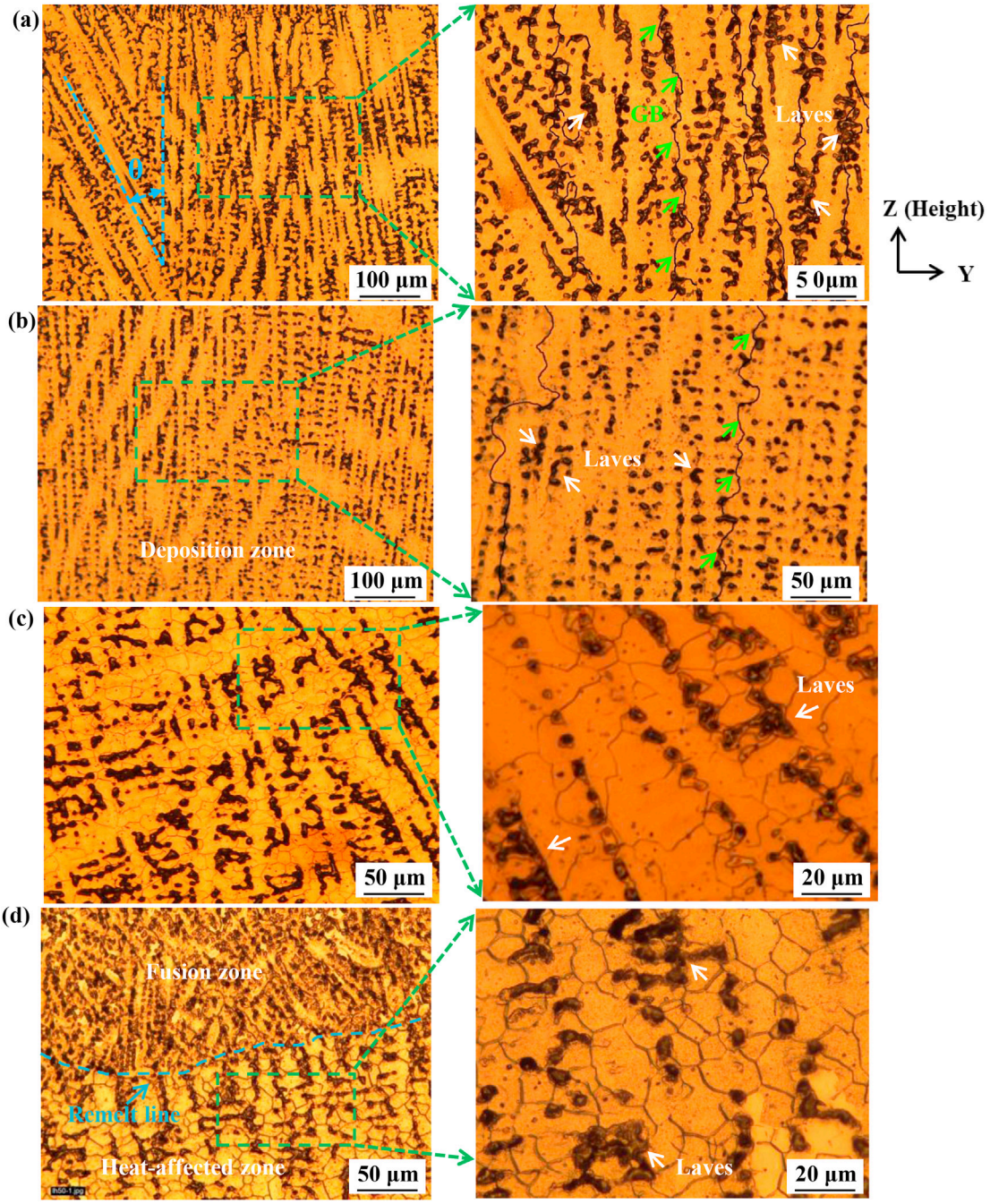

Fig. 10 – Microstructure variation under different conditions: (a) Bottom position of as-deposited; (b) Middle position of as-deposited; (c) 50 kN cold-rolled; (d) 75 kN cold-rolled.

precipitated at the inter-dendritic boundaries are the typical structures of the as-deposited IN-718. It can be seen that different positions of the as-deposited walls feature various characteristics of the columnar dendrites. The growth direction of the dendrites at middle positions of the as-deposited wall is parallel to the build direction; while there is a angle between the growth direction and the build direction at the bottom positions, as shown in Fig. 10(a) and (b). Furthermore, the average dendrite arm spacing of the dendrites increases with the increased build height. It increases from 89 μm at the bottom positions to 191 μm at the middle positions.

The variation of the dendrites at different positions of the deposited walls can be illustrated as follows: the formation of microstructure is related to the temperature gradient G and the solidification velocity R. The solidification structure will transform from cellular dendrites to columnar dendrites with the decreased ratio of G/R. The temperature gradient at the bottom positions is quite large due to the chilling effect of heat exchange between the material at the bottom positions of the deposited wall and the cold substrate. Moreover, the heat exchange with the cold substrate is generated in all directions, resulting in an angle between the growth direction of dendrites and the build direction. Wang [44] found the similar phenomenon that the growth directions of columnar dendrites were not necessarily parallel to the build direction and it changed slightly in side region of tracks. Meanwhile, many tiny and remelted secondary dendrite arms could also be found in this region as well as a number of fine cells at the inter-dendritic region. As a result, inclined grown columnar dendrites can be found at sides of the bottom material. With the proceeding of the deposition process, the temperature gradient decreases with the increased heat accumulation. Additionally, the directional heat exchange between the previously deposited material and the current deposited layer becomes dominant. Therefore, small temperature gradient and directional heat exchange both contribute to the formation of the directionally grown columnar dendrites with large arm spacing.

The cold rolling process obviously changes the microstructure distribution in the fusion zone and the heat-affected zone, as shown in Fig. 10(d). Mixed cell and columnar dendrites are generated in the fusion zone due to the remelting effect of the previous deposited material during the subsequent layer deposition. The columnar dendrites transform to equiaxed grains in the heat-affected zone after cold rolling process. With the increase of rolling force, the average grain size in the heat affected zone decreases accompanied by the improvement of the uniformity of the grains distribution. Additionally, the shape of the Laves phase of transforms from discrete islands into discrete disc due to the effect of fragmentation induced by the cold rolling process. Recrystallization is the main mechanism for the microstructure transformation and the grain refinement of the cold rolled sample. The deformation energy and dislocation density are significantly increased during the cold rolling process. As discussed in Section 3.3, the temperature of the previously deposited layer exceeds the solidus temperature during the subsequent layer deposition, which is much higher than the recrystallization temperature of IN-718 [45,46]. As a result, the heat input from the new layer deposition will trigger the static

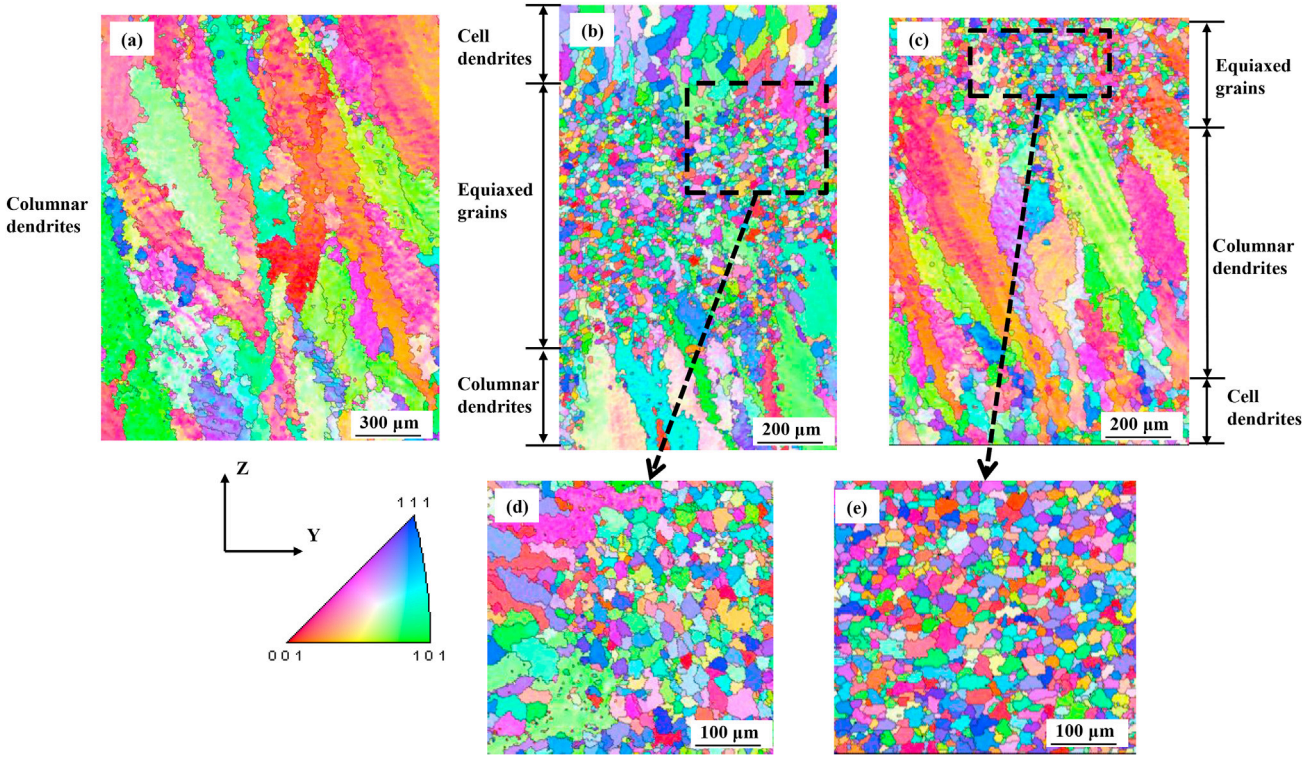

Fig. 11 – Grain orientation of: (a) As-deposited; (b) 50 kN cold-rolled; (c) 75 kN cold-rolled; (d) and (e) are high magnification of 50 kN and 75 kN, respectively.

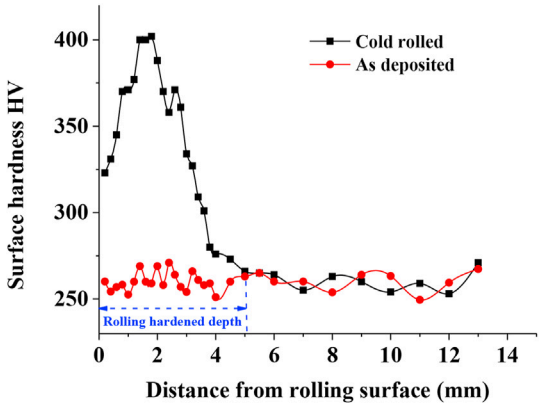

Fig. 12 – Hardness distribution of as-deposited and cold rolled samples.

recrystallization process and the columnar dendrites to equiaxed grains transformation (CET) occurs immediately. The accumulated deformation energy provides the driving force for the nucleation and growth of the recrystallized grains. The 75 kN rolled sample shows finer grains with more uniform distribution compared to that with 50 kN rolling force. It can be inferred that more nuclei is generated under the rolling force of 75 kN, resulting in more equiaxed grains with dispersive distribution. The grains transformation and grain refinement occur with the depletion of the deformation energy accumulated in the cold rolling process.

4.2. *Texture*

It is well known that the additively manufactured material shows strong texture, which results in the significant anisotropy of mechanical properties. The majority of the crystals in the as-deposited IN-718 show a preferred <001> orientation, indicating that the as-deposited material is strongly textured. This phenomenon is consistent with that in Oliveira's [47] result due to the directional heat exchange during WAAM deposition. The length of the columnar dendrites is several millimeters along the build direction due to the directional heat transfer in the WAAM deposition. The preferential grown columnar dendrites change to bands of small columnar dendrites, cell dendrites and equiaxed grains with random orientations under cold rolling process, as shown in Fig. 11 (b) and (c). This unique distribution of microstructure for the cold rolled samples can be explained as follows: based on Xu's results [48], the depth of the fusion zone for WAAM deposited

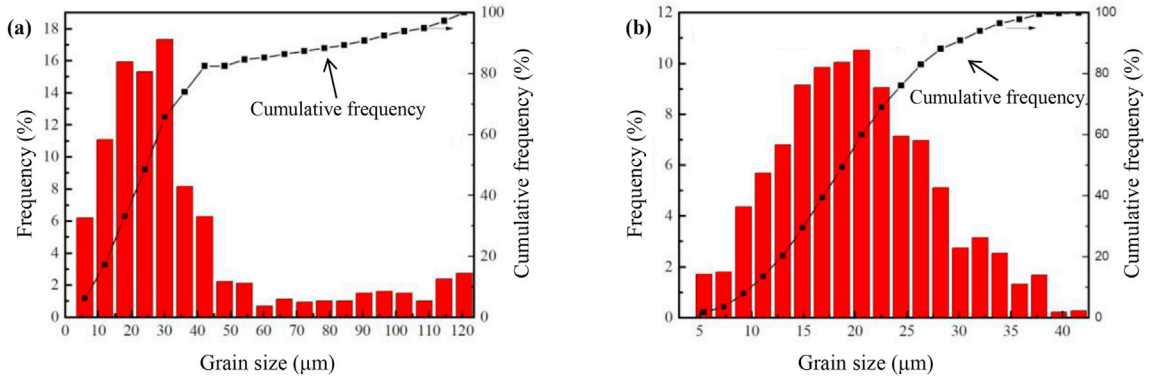

Fig. 13 – Grain size distribution of the equiaxed grains under: (a) 50 kN cold-rolled; (b) 75 kN cold-rolled.

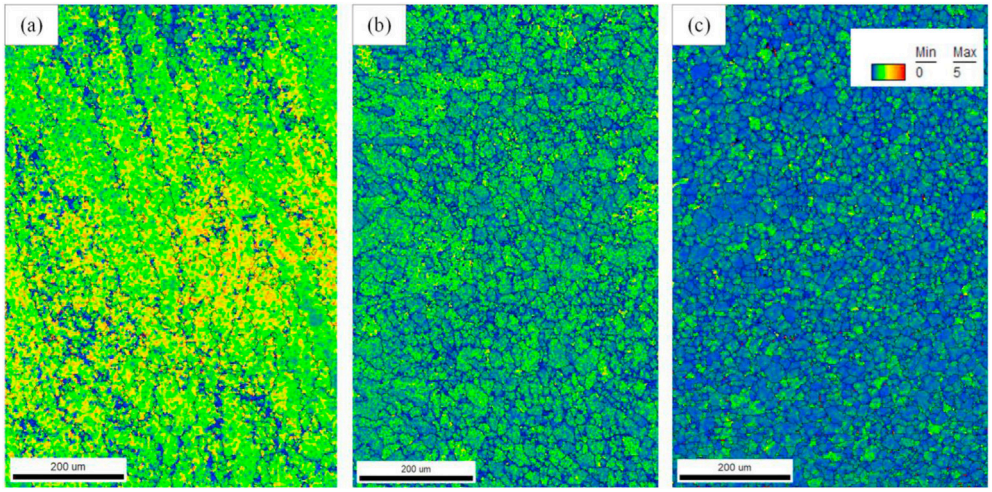

Fig. 14 – Kernel average misorientation of: (a) As-deposited; (b) 50 kN cold-rolled; (c) 75 kN cold-rolled.

IN718 is approximately equal to the layer height. After the rolling process, the microstructure shows different characteristic in the fusion zone and the heat-affected zone, as shown in Fig.10 and Fig.11. In order to promote recrystallization and grain refinement, the depth of the rolling hardened area should be larger than that of the depth of the fusion zone. The depth of the rolling hardened area is about 5 mm, which is larger than the depth of the fusion zone, as shown in Fig. 12. The hardness significantly increases under the cold rolling process and its peak value locates at the distance of 2 mm from the rolled surface, as shown in Fig. 12. Then it decreases with the increased depth and its value at the distance of 5 mm almost equals to the value of the deposited sample, which is defined as the rolling hardened depth. As a result, the mixed cell dendrites and small columnar dendrites will be generated in the remelting zone. Then, the accumulated dislocation density induced by the cold rolling process triggers the recrystallization and grain refinement in the heat-affected zone. It should be noted that the heat-affected zone consists of equiaxed grains at top positions and small columnar dendrites at bottom positions instead of equiaxed grains distributed throughout the whole heat-affected zone. Large deformation energy and high temperature are essential for the onset of the static recrystallization. It can be seen from Fig. 12 that the peak value of the hardness locates underneath the rolled surface and it decreases with the increased depth, indicating that the accumulated deformation energy decreases with the increased depth. Furthermore, the temperature also decreases with the increase of depth during the subsequent layer deposition process, as shown in the thermal

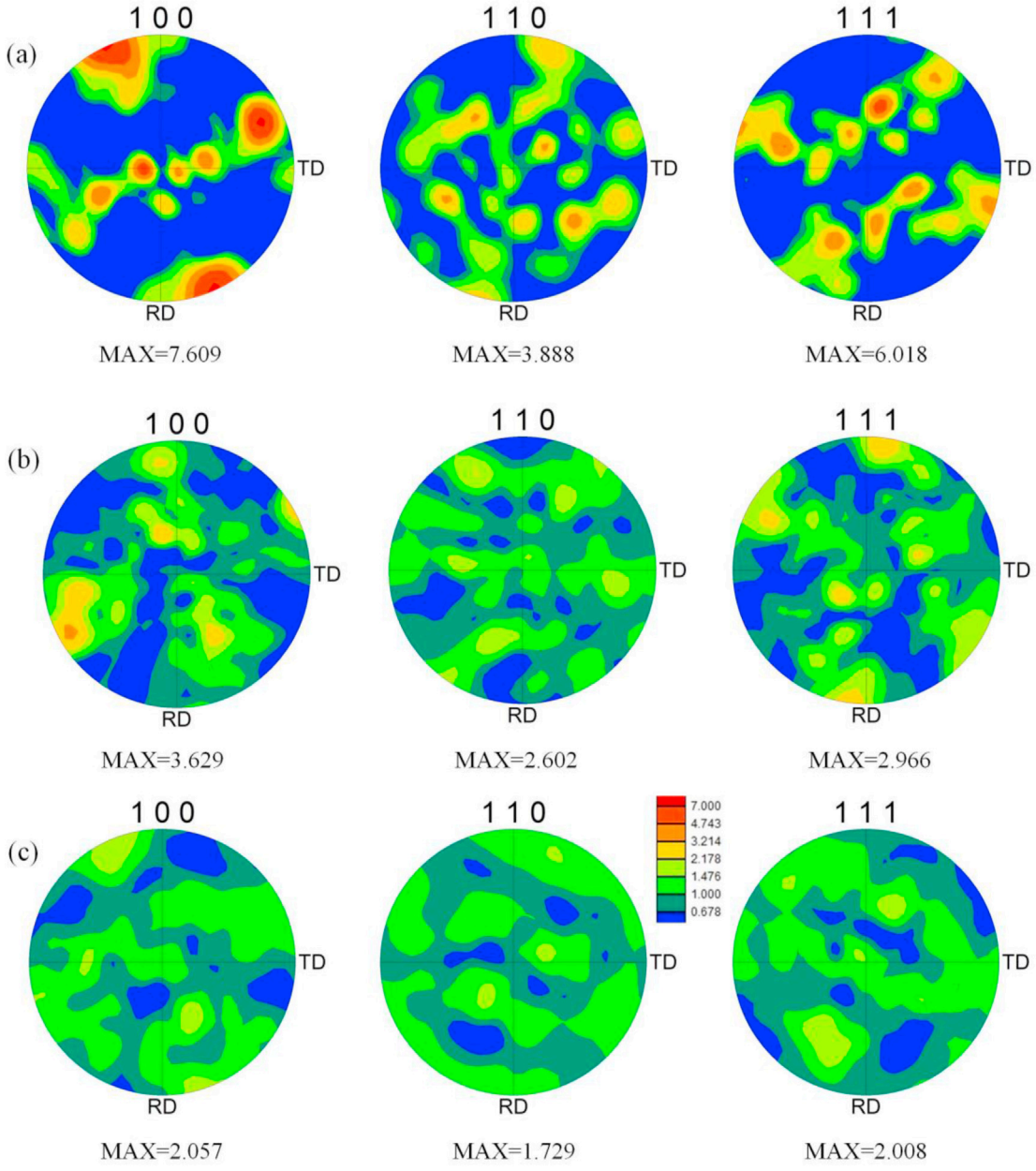

Fig. 15 – Pole figures of: (a) As-deposited; (b) 50 kN cold-rolled; (c) 75 kN cold-rolled.

cycles in Fig. 7. As a result, the recrystallization mainly occurs at the upper part of the rolled material and its recrystallized fraction decreases with the increased depth. Recrystallization hardly occurs at the bottom part of the rolled material due to its small strain and low temperature. Therefore, the columnar dendrites still exist at bottom part of the material. As a result, bands of equiaxed grains at top part and small columnar dendrites at bottom part are generated in heat-affected zone. Fig.13 shows the grain size distribution of the equiaxed grains in the heat affected zone for the cold rolled condition. Its average grain size is 30.7 μm and 19.2 μm with the rolling force of 50 kN and 75 kN, respectively. The cold rolled samples with the rolling force of 75 kN show a more uniform distribution of the grains as most of the grains are located at small sizes; while there are some large-scale grains (over 100 μm) for that with the rolling force of 50 kN. The cold rolling process induces the inhomogeneous distribution of strain, and the thermal cycles of WAAM deposition leads to the heterogeneous temperature distribution. Therefore, the mechanism for the inter-pass rolling is spatially and temporally heterogeneous work hardening and recrystallization.

Kernel average misorientation (KAM) is the average local misorientation between the target grain and its surrounding grains, representing the uniformity of the plastic strain [49,50]. The local misorientation is quite large for the as-deposited samples as the dislocation density inside the material increases due to the obvious residual stress induced by the WAAM deposition process. It decreases during the cold rolling process and its reduction increases with the increased rolling force, as shown in Fig. 14. The static recovery and static recrystallization significantly decrease the residual strain of the material. The dislocation polygonization of the deformed grains is generated during the static recovery process and it then transforms into equiaxed sub-grains. The migration and coalescence of the sub-grains during the static recrystallization will promote the growth of the recrystallized grains by depleting the deformation energy inside the material, thus significantly decreasing the local misorientation. It can be seen that the local misorientation in the cold rolled sample with the rolling force of 75 kN is more even than that of with the rolling force of 50 kN, which is consistent with the more uniformly distributed grains of the 75 kN rolled sample.

Pole figures is widely used to describe the texture density. Fig.15 shows the pole figures of the as-deposited and cold rolled samples. The as-deposited samples show the strongest intensity of 7.609 for the {100} family of grains oriented along

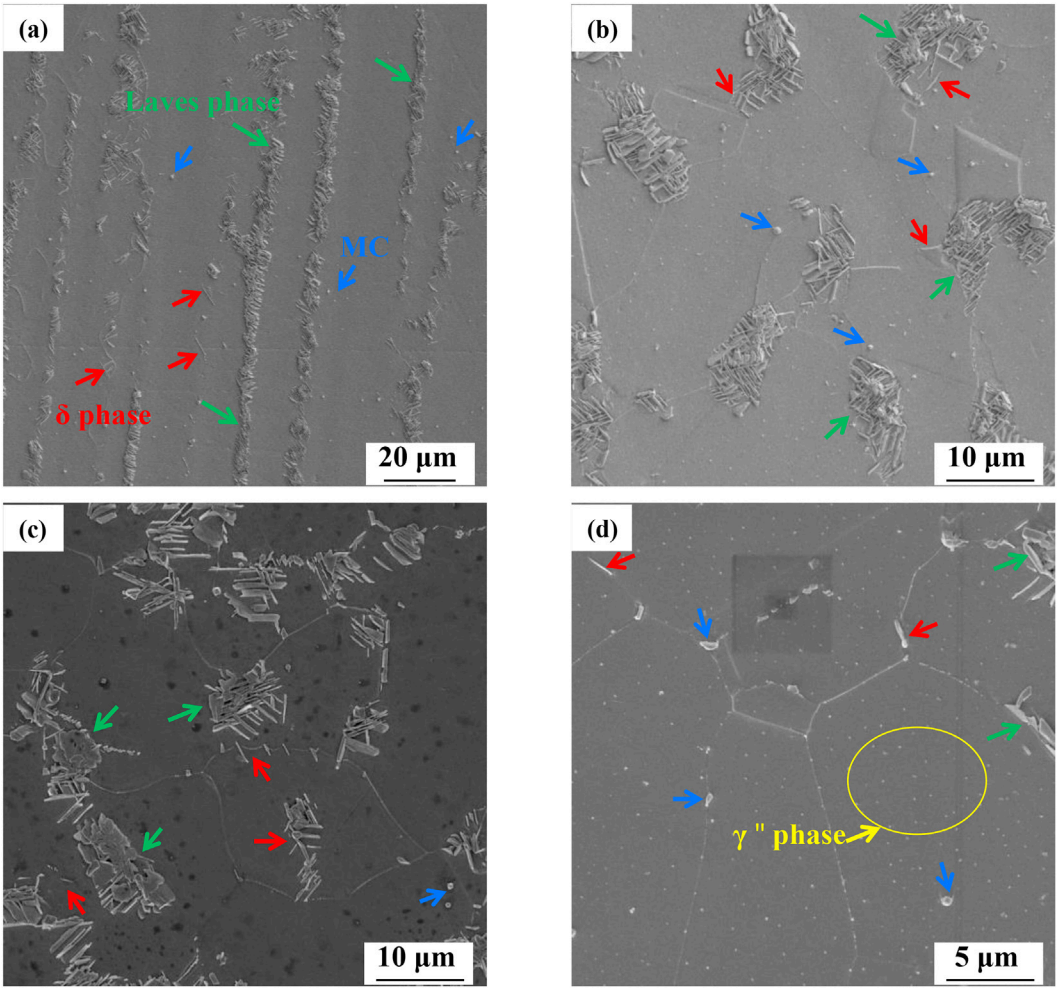

Fig. 16 – Precipitated phases distribution with heat treatment under conditions of: (a) As deposited; (b) 50 kN cold rolled; (c) 75 kN cold rolled; (d) High magnification of 75 kN cold rolled.

the transverse direction; while the intensity decreases to 3.629 and 2.057 for the cold rolled conditions with the rolling force of 50 kN and 75 kN, respectively. The as-deposited samples show a preferred <001> orientation and it is parallel to the direction with the largest temperature gradient during the deposition process, nevertheless, the cold rolled samples show a significant randomisation of texture. The directionally grown dendrites change to equiaxed grains under the cold rolling process, which significantly decreases the texture density.

4.3. *Precipitation*

Fig. 16 shows the precipitates distribution of the as-deposited and cold rolled conditions after heat treatment. Similar to the microstructure distribution, discrete islands of Laves phase with dendritic pattern, as well as acicular δ phases and circular MC carbides with discrete pattern are precipitated for the as-deposited samples. The grain boundaries change from dendritic pattern to equiaxed pattern, and some acicular δ phases appear at the grain boundary and also cluster around the Laves phase after cold rolling process. The size of the Laves phase and δ phase can be calculated with the software of Image J. The length of the Laves phase is 54.5 ± 17.2 μm for as-deposited sample, which decreases to 13.5 ± 2.7 μm and 8.4 ± 2.2 μm with the rolling force of 50 kN and 75 kN, respectively. Meanwhile, the length of the δ phase decreases from 6.0 ± 0.7 μm to 2.5 ± 0.4 μm and 1.7 ± 0.3 μm, respectively, as shown in Fig. 16 (a)–(c). Therefore, discrete islands of Laves phase and the δ phase are broken into small pieces under cold rolling and its size decreases with the increased rolling force. Neverthless, the Laves phase and MC carbides still exist after cold rolling process. The dissolving temperature of the Laves phase is 1093 °C according to AMS 5383 [51] and 1150 °C in Sohrabi's study [52] for cast IN-718, 1050 °C for laser powder fed additively manufactured material [53], and 1100 °C for plasma additively manufactured material [54]. The liquidus temperature of MC carbides is 1340 °C [55]. The solution temperature is 970 °C and it is much lower than the dissolving temperatures of Laves phase and MC carbides, therefore, they can not be completely eliminated during the cold rolling with the heat treatment [56,57]. The precipitation of δ phase occurs between 860 °C and 995 °C with its peak value of fraction at 900 °C [58–60]; while the precipitation temperature of γ″ phase ranges from 600 °C to 870 °C with its peak value around 740 °C. Some small white and circular phases precipitate at the grain boundaries and the grain interiors, which proves to be the strengthening γ″ phase based on EDS analysis, as shown in Fig. 16 (d). Additionally, the thermal cycles in the subsequent layers deposition provides the transient aging effect to the previous deposited material, thus inducing the precipitation of the δ phase and the γ″ phase.

Table 5 – Tensile test results of IN718 at room temperature.

	UTS/MPa	YS/MPa	Elongation (%)
WAAM deposited	840.7 ± 13.3	472.5 ± 9.5	26.3 ± 1.1
50 kN cold rolled	971.7 ± 19	724.3 ± 18.2	24.2 ± 1.8
75 kN cold rolled	1075.2 ± 15.4	775.2 ± 14.2	22.3 ± 1.2

The tensile test at room temperature for the WAAM deposited and cold rolled samples are conducted, as shown in Table 5. The as-deposited samples show lower UTS and YS, but higher elongation compared to that in the cold rolled samples. The cold-rolling increases the strength and reduces the elongation. The increase in strength and the corresponding reduction in elongation both increase with increasing rolling force.

5. Conclusions

Numerical models of Inconel 718 in WAAM deposition were established and the location-related thermal history and temperature variation were analyzed, which were verified by the experiments using the thermocouples and the infrared camera. The effect of thermal cycles on the distributions of microstructure, texture and precipitates were investigated by experimental methods.

(1)The latent heat due to the solidification was considered in the three-dimensional FEM and the arc-shape deposited bead of WAAM deposition was simulated. The WAAM deposition shows repeated thermal cycles and different regions of the deposited layers features a different thermal history due to its inherent characteristics of rapid heating, melting and cooling processes. The peak temperature of the thermal cycles decreases with the proceeding of the deposition process; while the trough values of the temperature first increases in the previous several layers deposition and then decreases. The heating rate is always higher than the cooling rate in each layer deposition and they both decrease with the proceeding of the deposition process.

(2)The microstructure of the WAAM deposition and hybrid technology was comparatively analyzed using OM and EBSD methods. The as-deposited samples show extensively grown columnar dendrites and its average dendrite arm spacing increases with the increased build height due to the different heat accumulation conditions at different positions of the wall. The angle between the growth of the columnar dendrites and the build direction varies with the increased build height due to the difference of the heat exchange directions. The heat exchange between the bottom material and the cold substrate is generated in all directions while it changes to directional heat exchange with the increased build height. The cold rolling contributes to the transformation from columnar dendrites to equiaxed grains and the average grain size of the equiaxed grains decreases with the increased rolling force. It decreases from 30.7 μm to 19.2 μm with the rolling force of 50 kN–75 kN. The as-deposited samples show strongly textured columnar dendrites in preferred <001> orientation with the intensity of 7.609, and it changes to equiaxed grains in random orientation in the heat-affected zone with the intensity of 3.629 and 2.057 under the rolling force of 50 kN–75 kN, respectively.

(3)The as-deposited samples show dendritic pattern of precipitates with discrete islands of Laves phase, acicular δ phases and circular MC carbides. The grain boundaries

change from dendritic pattern to equiaxed pattern, and some acicular δ phases appear at the grain boundary and also cluster around the Laves phase after cold rolling process. The cold rolling is beneficial for the precipitation of the strengthening γ" phase at the grain boundaries and the grain interiors.

(4)The relationship between the location-related thermal cycles and the microstructure variation was discussed. The dendrite size increased with the increased heat input induced by the heat accumulation.

(5)The mechanism for the intergrated inter-pass rolling consisted of work hardening and recrystallization. Meanwhile, the rolling deformation and the recrystallization were heterogeneous, which was related to the positions and the deposition time of the wall.

Declaration of Competing Interest

The authors declare that they have no known competing financial interests or personal relationships that could have appeared to influence the work reported in this paper.

Acknowledgements

The authors wish to acknowledge the financial support from the State Key Laboratory for High Performance Complex Manufacturing, Central South University (ZZYJKT2021-05).

REFERENCES

[1] Tang YL, Ye X, Ding LC, Zhang PL, Fu KJ. High-temperature tensile properties and interface structure of Ni–Fe dissimilar butt joints welded using the cold metal transfer process. J Mater Res Technol 2020;9:15023–33.

[2] Gallo F, Azevedo L, Labre C, Araújo L, Dille J, Luiz Almeida L. Correlation between grain boundary character distribution and δ-phase precipitation in nickel-based superalloy 718. J Mater Res Technol 2019;9:1801–8.

[3] Zhang L, Shi X, Li N, Zhao L, Chen W. Heterogeneities of microstructure and mechanical properties for Inconel 718 strut tensile sample fabricated by selective laser melting. J Mater Res Technol 2021;12:2396–406.

[4] Liu Z, Zhu Q, Zhang X. Tailoring microstructure and mechanical property of laser powder deposited Inconel 718 superalloy via hybrid processing strategies. J Manuf Process 2021;68:1837–48.

[5] Alizadeh-Sh M, Marashi SPH, Ranjbarnodeh E, Shoja-Razavi R, Oliveira JP. Prediction of solidification cracking by an empirical-statistical analysis for laser cladding of Inconel 718 powder on a non-weldable substrate. Opt Laser Technol 2020;128:106244.

[6] Zhang S, Lin X, Wang L, Yu X, Huang W. Strengthening mechanisms in selective laser-melted Inconel 718 superalloy. Mater Sci Eng, A 2021;812:141145.

[7] Dleker KM, Erdogan A, Yener T, Karaoglanl AC, Zeytin S. Enhancing the wear and oxidation behaviors of the Inconel 718 by low temperature aluminizing. Surf Coating Technol 2021;412:127069.

[8] Shim DS, Lee H, Son Y, Oh WJ. Effects of pre- and post-repair heat treatments on microstructure and tensile behaviors of 630 stainless steel repaired by metal additive manufacturing. J Mater Res Technol 2021;13:980–99.

[9] Lopes JG, Machado CM, Duarte VR, Rodrigues TA, Santos TG, Oliveira JP. Effect of milling parameters on HSLA steel parts produced by Wire and Arc Additive Manufacturing (WAAM). J Manuf Process 2020;59:739–49.

[10] Rodrigues TA, Bairrão N, Farias F, Shamsolhodaei A, Shen J, Zhou N, et al. Steel-copper functionally graded material produced by twin-wire and arc additive manufacturing (T-WAAM). Mater Des 2022;213:110270.

[11] Ramalho A, Santos TG, Bevans B, Smoqi Z, Rao P, Oliveira JP. Effect of contaminations on the acoustic emissions during wire and arc additive manufacturing of 316L stainless steel. Addit Manuf 2021;51:102585.

[12] Chen X, Kong F, Fu Y, Zhao X, Li R, Wang G, et al. A review on wire-arc additive manufacturing: typical defects, detection approaches, and multisensor data fusion-based model. Int J Adv Manuf Technol 2021;117:707–27.

[13] Guo C, Ying M, Dang H, Hu R, Chen F. Microstructural and intergranular corrosion properties of Inconel 625 superalloys fabricated using wire arc additive manufacturing. Mater Res Express 2021;8:35103.

[14] Faraji AH, Maletta C, Barbieri G, Cognini F, Bruno L. Numerical modeling of fluid flow, heat, and mass transfer for similar and dissimilar laser welding of Ti-6Al-4V and Inconel 718. Int J Adv Manuf Technol 2021;114(3):899–914.

[15] Su C, Chen X, Konovalov S, Singh R, Jayalakshmi S, Huang L. Effect of deposition strategies on the microstructure and tensile properties of wire arc additive manufactured Al-5Si alloys. J Mater Eng Perform 2021;30:2136–46.

[16] Ke WC, Oliveira JP, Cong BQ, Ao SS, Qi ZW, Peng B, et al. Multi-layer deposition mechanism in ultra high-frequency pulsed wire arc additive manufacturing (WAAM) of NiTi shape memory alloys. Addit Manuf 2022;50:102513.

[17] Graf M, Hälsig A, Höfer K, Awiszus B, Mayr P. Thermo-mechanical modelling of wire-arc additive manufacturing (WAAM) of semi-finished products. Metals 2018;8:1009.

[18] Singh SN, Chowdhury S, Nirsanametla Y, Deepati AK, Prakash C, Singh S, et al. A comparative analysis of laser additive manufacturing of high layer thickness pure Ti and Inconel 718 alloy materials using finite element method. Materials 2021;14:876.

[19] Manurung Y, Prajadhiana K, Adenan M, Awiszus B, Haelsig A. Analysis of material property models on WAAM distortion using nonlinear numerical computation and experimental verification with P-GMAW. Arch Civ Mech Eng 2021;21:1–13.

[20] Ding D, Zhang S, Lu Q, Pan Z, Wang K. The well-distributed volumetric heat source model for numerical simulation of wire arc additive manufacturing process. Mater Today Commun 2021;27:102430.

[21] Sun J, Hensel J, Kohler M, Dilger K. Residual stress in wire and arc additively manufactured aluminum components. J Manuf Process 2021;65:97–111.

[22] Yang D, Xiong J, Li R. Numerical study of heat transfer characteristics in positional wire and arc additive manufacturing. Rapid Prototyp J 2020;26:1627–35.

[23] Fang X, Zhang L, Yang J, Bai H, Zhao L, Huang K, et al. Effect of characteristic substrate parameters on the deposition geometry of CMT additive manufactured Al-6.3%Cu alloy. Appl Therm Eng 2019;162:114302.

[24] Li R, Xiong J. Influence of interlayer dwell time on stress field of thin-walled components in WAAM via numerical simulation and experimental tests. Rapid Prototyp J 2019;25:1433–41.

[25] Knezovi N, Garai I, Juri I. Influence of the interlayer temperature on structure and properties of wire and arc

additive manufactured duplex stainless steel product. Materials 2020;13(24):5795.
[26] Xiong J, Lei Y, Li R. Finite element analysis and experimental validation of thermal behavior for thin-walled parts in GMAW-based additive manufacturing with various substrate preheating temperatures. Appl Therm Eng 2017;126:43–52.
[27] Benakis M. Current mode effects on weld bead geometry and heat affected zone in pulsed wire arc additive manufacturing of Ti-6-4 and Inconel 718. J Manuf Process 2020;60:61–74.
[28] Ge J, Jian L, Lei Y, Fu H. Location-related thermal history, microstructure, and mechanical properties of arc additively manufactured 2Cr13 steel using cold metal transfer welding. Mater Sci Eng, A 2017;715:144–53.
[29] Wu B, Ding D, Pan Z, Cuiuri D, Li H, Han J, et al. Effects of heat accumulation on the arc characteristics and metal transfer behavior in Wire Arc Additive Manufacturing of Ti6Al4V. J Mater Process Technol 2017;250:304–12.
[30] Rodrigues TA, Duarte V, Avila JA, Santos TG, Miranda RM, Oliveira JP. Wire and Arc additive manufacturing of HSLA steel: effect of thermal cycles on microstructure and mechanical properties. Addit Manuf 2019;27:440–50.
[31] Kindermann R, Roy M, Morana R, Prangnell P. Process response of Inconel 718 to wire + arc additive manufacturing with cold metal transfer. Mater Des 2020;195:109031.
[32] Ge J, Ma T, Han W, Yuan T, Lin J. Thermal-induced microstructural evolution and defect distribution of wire-arc additive manufacturing 2Cr13 part: numerical simulation and experimental characterization. Appl Therm Eng 2019;163:114335.
[33] Hejripour F, Binesh F, Hebel M, Aidun D. Thermal modeling and characterization of wire arc additive manufactured duplex stainless steel. J Mater Process Technol 2019;272:58–71.
[34] Tanvir A, Ahan R, Seo G, Vates B, Lee C, Liaw P, et al. Phase stability and mechanical properties of wire + arc additively manufactured H13 tool steel at elevated temperatures. J Mater Sci Technol 2021;67:80–94.
[35] Gao C, Chen X, Su C, Chen X. Location dependence of microstructure and mechanical properties on wire arc additively manufactured nuclear grade steel. Vacuum 2019;168:108818.
[36] Bai JY, Fan CL, Lin SB, Yang CL, Dong BL. Effects of thermal cycles on microstructure evolution of 2219-Al during GTA-additive manufacturing. Int J Adv Manuf Technol 2016;87:2615–23.
[37] Gokhale N, Kala P. Thermal analysis of TIG-WAAM based metal deposition process using finite element method. Mater Today Proc 2021;44:453–9.
[38] Geng R, Du J, Wei Z, Ma N. Multiscale modelling of microstructure, micro-segregation, and local mechanical properties of Al-Cu alloys in wire and arc additive manufacturing. Addit Manuf 2020;36:101735.
[39] Goldak J, Bibby M, Moore J, House R, Patel B. Computer modeling of heat flow in welds. Metall Trans B 1986;17(3):587–600.
[40] Lu X, Zhou YF, Xing XL, Wang B, Yang QX, Gao SY. Surface additive manufacturing of Ni-based superalloy/H13 steel system by laser depositing: microstructure, microhardness and flexural response. Surf Coating Technol 2018;337:525–35.
[41] Lu X, Zhou YF, Xing XL, Wang B, Yang QX, Gao SY. Open-source wire and arc additive manufacturing system: formability, microstructures, and mechanical properties. Int J Adv Manuf Technol 2017;93:2145–54.
[42] Goldak J, Chakravarti AP, Bibby M. A new finite element model for welding heat sources. Metall Mater Trans B 1984;2:299–305.
[43] Oliveira JP, Lalonde AD, Ma J. Processing parameters in laser powder bed fusion metal additive manufacturing. Mater Des 2020;193:108762.
[44] Wang K, Liu Y, Sun Z, Lin J, Xu B. Microstructural evolution and mechanical properties of Inconel 718 superalloy thin wall fabricated by pulsed plasma arc additive manufacturing. J Alloys Compd 2019;819:152936.
[45] Chen XM, Lin YC, Wu F. EBSD study of grain growth behavior and annealing twin evolution after full recrystallization in a nickel-based superalloy. J Alloys Compd 2017;724:198–207.
[46] Lin YC, Chen XM, Chen MS, Zhou Y, Wen DX, He DG. A new method to predict the metadynamic recrystallization behavior in a typical nickel-based superalloy. Appl Phys A 2016;122:1–14.
[47] Oliveira JP, Curado TM, Zeng Z, Rossinyol E, Park JM, Schell N, et al. Gas tungsten arc welding of as-rolled CrMnFeCoNi high entropy alloy. Mater Des 2020;189:108505.
[48] Xu X, Ganguly S, Ding J, Seow C, Williams S. Enhancing mechanical properties of wire+ arc additively manufactured INCONEL 718 superalloy through in-process thermomechanical processing. Mater Des 2018;160:1042–51.
[49] Kamaya M. Measurement of local plastic strain distribution of stainless steel by electron backscatter diffraction. Mater Char 2009;60:125–32.
[50] Kamaya M. Characterization of microstructural damage due to low-cycle fatigue by EBSD observation. Mater Char 2009;60:1454–62.
[51] Zhang D, Niu W, Cao X, Liu Z. Effect of standard heat treatment on the microstructure and mechanical properties of selective laser melting manufactured Inconel 718 superalloy. Mater. Sci. Eng. A-Struct. 2015;644:32–40.
[52] Sohrabi MJ, Mirzadeh H, Rafiei M. Solidification behavior and laves phase dissolution during homogenization heat treatment of Inconel 718 superalloy. Vacuum 2018;154:235–43.
[53] Sui S, Tan H, Chen J, Zhong C, Li Z, Fan W, et al. The influence of laves phases on the room temperature tensile properties of Inconel 718 fabricated by powder feeding laser additive manufacturing. Acta Mater 2019;164:413–27.
[54] Seow CE, Coules HE, Wu G, et al. Wire + Arc Additively Manufactured Inconel 718: effect of post-deposition heat treatments on microstructure and tensile properties. Mater Des 2019;183:108157.
[55] Wang X, Chou K. The effects of stress relieving heat treatment on the microstructure and residual stress of Inconel 718 fabricated by laser metal powder bed fusion additive manufacturing process. J Manuf Process 2019;48:154–63.
[56] Careri F, Umbrello D, Essa K, Attallah MM, Imbrogno S. The effect of the heat treatments on the tool wear of hybrid Additive Manufacturing of IN718. Wear 2021;470–471:203617.
[57] Tucho WM, Hansen V. Studies of post-fabrication heat treatment of L-PBF-inconel 718: effects of hold time on microstructure, annealing twins, and hardness. Metals 2021;11(2):266.
[58] Cao GH, Sun TY, Wang CH. Investigations of γ', γ'' and δ precipitates in heat-treated Inconel 718 alloy fabricated by selective laser melting. Mater Char 2018;136:398–406.
[59] Zhang H, Li C, Guo Q, Ma Z, Huang Y, Li H, et al. Hot tensile behavior of cold-rolled Inconel 718 alloy at 650 °C the role of δ phase. Mater Sci Eng, A 2018;722:136–46.
[60] Anderson M, Thielin AL, Bridier F, Bocher P, Savoie J. δ Phase precipitation in Inconel 718 and associated mechanical properties. Mater Sci Eng, A 2017;679:48–55.

https://dspace.org/

Study on location-related thermal cycles and microstructure variation of additively manufactured Inconel 718

Zhang, Tao; Li, Huigui; Gong, Hai; Wu, Yunxin; Chen, Xin ...

2022-04-04
Elsevier
https://doi.org/10.1016/j.jmrt.2022.03.178
Zhang T, Li H, Gong H, et al., (2022) Study on location-related thermal cycles and microstructure variation of additively manufactured Inconel 718. Journal of Materials Research and Technology, Volume 18, May-June 2022, pp. 3056-3072

Downloaded from a DSpace repository. https://dspace.org/